

Quantitative electron microscopy and fluorescence spectroscopy of the membrane distribution of influenza hemagglutinin

Samuel T. Hess,¹ Mukesh Kumar,¹ Anil Verma,¹ Jane Farrington,¹ Anne Kenworthy,² and Joshua Zimmerberg¹

¹Laboratory for Cellular and Molecular Biophysics, National Institute of Child Health and Human Development, National Institutes of Health, Bethesda, MD 20892

²Department of Molecular Physiology and Biophysics and Department of Cell and Developmental Biology, Vanderbilt University School of Medicine, Nashville, TN 37232

Although lipid-dependent protein clustering in biomembranes mediates numerous functions, there is little consensus among membrane models on cluster organization or size. Here, we use influenza viral envelope protein hemagglutinin (HA₀) to test the hypothesis that clustering results from proteins partitioning into preexisting, fluid-ordered “raft” domains, wherein they have a random distribution. Japan HA₀ expressed in fibroblasts was visualized by electron microscopy using immunogold labeling and probed by fluorescence resonance energy transfer (FRET). Labeled HA coincided with electron-dense, often noncircular membrane patches. Poisson and K-test (Ripley, B.D.

1977. *J. R. Stat. Soc. Ser. B.* 39:172–212) analyses reveal clustering on accessible length scales (20–900 nm). Membrane treatments with methyl- β -cyclodextrin and glycosphingolipid synthesis inhibitors did not abolish clusters but did alter their pattern, especially at the shortest lengths, as was corroborated by changes in FRET efficiency. The magnitude and density dependence of the measured FRET efficiency also indicated a non-random distribution on molecular length scales (\sim 6–7 nm). This work rules out the tested hypothesis for HA over the accessible length scales, yet shows clearly how the spatial distribution of HA depends on lipid composition.

Introduction

The landmark discovery that enveloped viruses can acquire membranes with differential composition, as they bud out of different regions of the plasma membrane (van Meer and Simons, 1982), forms some of the earliest evidence that enveloped viruses exploit glycosphingolipid and cholesterol-enriched domains known as lipid rafts as part of the viral life cycle (Suomala, 2002). Subsequent studies have shown that there are two different lipid domains in the viral envelope (Bukrinskaya et al., 1987), and that HA, the major envelope protein of influenza, is insoluble in cold nonionic detergent, now recognized as a biochemical fingerprint of raft-resident proteins (Skibbens et al., 1989). Infectivity of HIV, Ebola, and influenza, as well as bud-

ding of influenza, depend on sphingolipid and cholesterol-rich membrane domains (Scheiffele et al., 1999; Nguyen and Hildreth, 2000; Ono and Freed, 2001; Bavari et al., 2002; Sun and Whittaker, 2003) that are putatively disrupted by removal of cellular cholesterol by methyl- β -cyclodextrin (Kilsdonk et al., 1995). HA-mediated cell–cell fusion, viral infectivity, and budding were also found to depend on HA (H3 subtype) transmembrane domain sequence, and correlated with the clustering of HA in the plasma membrane as detected by EM (unpublished data and Takeda et al., 2003). These biological effects are thought to result from redistribution of the HA and lipid after disruption of putative “raft” domains that presumably restrict lateral diffusion and thereby maintain a high local concentration of HA (Takeda et al., 2003).

The proposed functions of lipid rafts are not limited to viral entry and exit from cells. A crescendo of publications on membrane microdomains suggests they are important in a variety of cell signaling and membrane trafficking pathways. Despite this, there is considerable controversy on the existence, size, life time, and physiological importance of putative domains (Simons and Ikonen, 1997; Edidin, 2001, 2003; Anderson and Jacobson,

Correspondence to Joshua Zimmerberg: joshz@helix.nih.gov

S. Hess' present address is Department of Physics and Astronomy, University of Maine, Orono, ME 04469.

Abbreviations used in this paper: $A(\theta)$, distribution of angles; C_{log} , Ripley's K-test 99% confidence interval; f_{clus} , fraction of clustering; FRET, fluorescence resonance energy transfer; $L(r) - r$, Ripley's K-test metric; M β CD, methyl- β -cyclodextrin; $N(r)$, nearest neighbor distance distribution; PDMP, 1-phenyl-2-decanoylamino-3-morpholino-1-propanol; PPMP, 1-phenyl-2-palmitoyl-amino-3-morpholino-1-propanol; ρ_{nn} , most common nearest neighbor distance; r_0 , correlation length.

The online version of this article includes supplemental material.

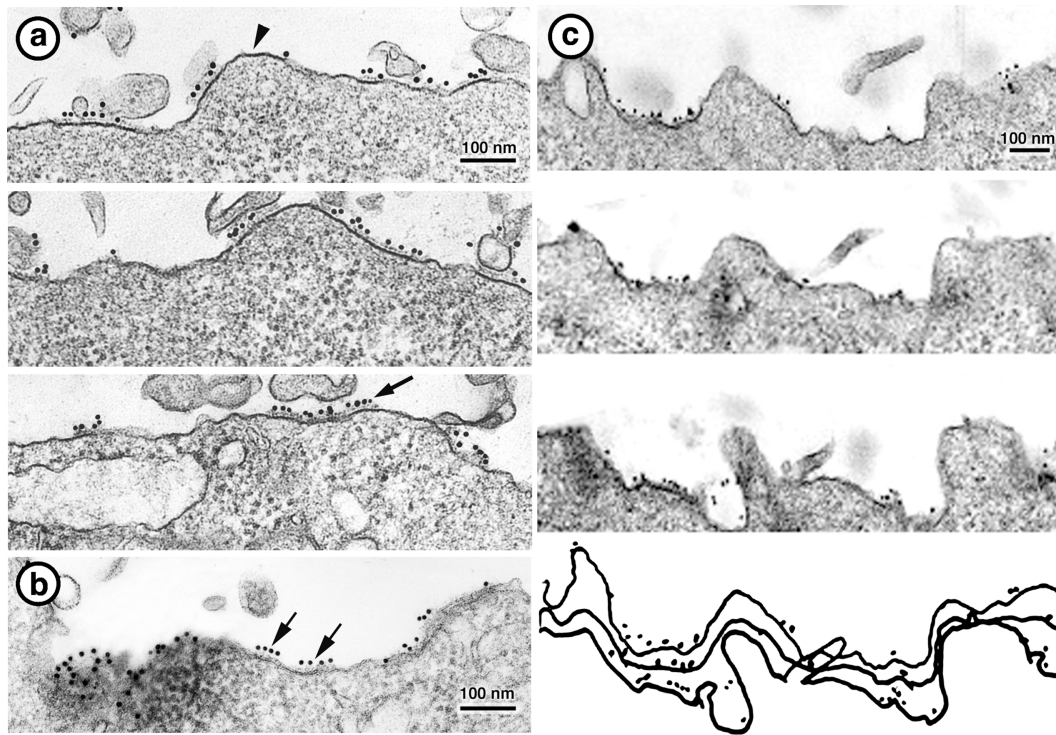


Figure 1. **Ultrathin sections show clustered distribution of HA in one dimension.** Whole cells were immunolabeled from the outside. We then specifically examined the distribution of the gold at the plasma membrane. Ultrathin (50 nm) cross sections of whole cells were prepared of (a) untreated HAB2 cells, fixed before labeling with α -HA mouse primary and 10-nm colloidal gold conjugated secondary antibodies. (b) Untreated HAB2, immunostained at 4°C and then fixed. (c) Serial cross sections (50 nm) and the resulting reconstructed pattern of gold particles on an untreated HAB2 cell surface, fixed before immunostaining. Bar, 100 nm. Gold clusters were always over darker membranes (arrows), whereas dark areas need not have gold on them (arrowhead).

2002; Fujiwara et al., 2002; Nakada et al., 2003; Kenworthy et al., 2004; Sharma et al., 2004). Here, we use HA to test some of the predictions of raft models, focusing on the idea of a fluid lipid domain. We expect fluid domains to have distinct, testable properties, including rounded boundaries and preferential partitioning of certain proteins and lipids into those domains. In this work, we set out to test whether HA is found in fluid domains that are ideally mixed. One hypothesis for HA clustering would be a favorable partition coefficient between domain and nondomain membrane. This hypothesis predicts that within each domain the lateral distribution of protein will be random, but at a concentration that is proportional to the average membrane density. Thus, another prediction is that the distance between HAs will decrease as average membrane density increases. On the other hand, an alternate hypothesis is that the assembly of domains is due to self-assembly of molecular complexes, in which case there need not be any fixed size, as this will depend on the relative on- and off-rates of dynamic cluster assembly and disassembly. Self-assembled complexes would also allow for average HA-HA distances that do not depend on the average HA density. Self-assembly of protein-lipid complexes due to specific intermolecular interactions would also provide a diversity of distinct membrane domains with different protein and lipid compositions, each serving potentially different biological functions. In agreement with such a mechanism, raft markers such as Thy-1, GM1, and palmitoylated LAT have been observed previously to be found in distinct membrane clusters that are not colocalized (Wilson et al., 2004). In contrast, work by Shvartsman et al. (2003) shows that GPI-

anchored BHA-PI and GPI-GFP can coexist in microdomains with wt-HA. Thus, there are presumably selective mechanisms that determine the partitioning of specific components into a given type of microdomain. Finally, there is the set of hypotheses that includes all types of membrane domains other than ideally mixed fluid domains and self-assembled complexes.

We determined the lateral organization of HA on plasma membranes of stably transfected fibroblast cells (the HAB2 cell line) (Ellens et al., 1990) at length scales that span three orders of magnitude. Our results for influenza HA (H2 subtype) are inconsistent with partitioning of trimers into domains with random intra-domain distributions. We hypothesize that the longer and shorter length scale regimes for HA mediate two of its crucial biological functions: viral assembly and viral entry, respectively. We further hypothesize that lipid-dependent assembly of HA achieves these functions by first creating pre-envelope domains of specific lipids and proteins on the plasma membrane before interacting with influenza matrix protein M1 for budding of complete virions; this assembly may be important for fusion.

Results

Thin sections and membrane sheets imaged en face show a nonrandom distribution of influenza HA as visualized by immunogold EM

HAB2 fibroblast cell plasma membrane ultrathin (50 nm) sections were prepared by thin section, and membrane sheets were

prepared by the “rip-flip” method of Sanan and Anderson (1991). Treated membranes from cells grown in culture were prepared by incubation with compounds that alter the membrane lipid composition before sectioning or rip-flip. Treatments include methyl- β -cyclodextrin (M β CD) (Kilsdonk et al., 1995), used to remove cholesterol from the cell membranes; 10 μ M 1-phenyl-2-decanoylamino-3-morpholino-1-propanol (PDMP); and 10 μ M 1-phenyl-2-palmitoyl-amino-3-morpholino-1-propanol (PPMP) (Abe et al., 1992, 1996). PDMP and PPMP inhibit glycosphingolipid synthesis, but at 25 μ M also are reported to reduce sphingomyelin in cells (Rosenwald et al., 1992; Chen et al., 1995) and in hippocampal neurons (Hisaki et al., 2004).

Membrane sections were labeled with α -HA primary antibody, followed by 10-nm colloidal gold-conjugated secondary antibody, and were then imaged by EM (Fig. 1). Membranes fixed before labeling (Fig. 1 a), membranes labeled before fixing (Fig. 1 b), and membranes cut in 50-nm serial sections (Fig. 1 c) all showed a highly nonrandom distribution of HA. Note that the membrane bilayer frequently appears darkened in regions near where a gold particle is bound. Both membranes treated with M β CD, PDMP, and PPMP, and untreated membranes showed a clustered distribution of HA (unpublished data). Frequently, electron-dense material was visible between the gold particles and the immediately adjacent plasma membrane.

To increase the number of gold particles observed and to visualize their distribution more easily in two dimensions, HAb2 cell membrane sheets prepared by the method of Sanan and Anderson (1991) were labeled with the same α -HA primary and 10-nm colloidal gold-conjugated secondary antibodies and imaged en face (Fig. 2 and Fig. 3). Clustering was visible on many length scales, and generally, clusters coincided with electron-dense membrane regions that were observed in the presence or absence of immunogold but not in grid regions without membrane or where the membrane had locally torn away (unpublished data). Generally, these electron-dense regions had irregular boundaries resembling small dark islands in a light sea or other self-similar shapes, although occasionally they showed rounded boundaries containing clusters of HA. Gold particles were correlated with the electron-dense regions (see image analysis method 6) on length scales roughly less than correlation length (r_0) $\sim 92 \pm 16$ nm in selected untreated membranes and $r_0 \sim 136 \pm 80$ nm in M β CD-treated membranes. In some cases the clusters appeared to have triangular or hexagonal symmetry (Fig. 2, arrow) reminiscent of packing of circles or spheres. To better quantify the HA distribution, the x-y coordinates of each immunogold particle were tabulated and analyzed by a number of methods.

Poisson analysis

As a test of randomness of the membrane distribution of HA, we performed Poisson analysis of the frequency distribution of the number of immunogold particles within boxes of a given size spaced uniformly across imaged areas. This analysis revealed quantitatively ($\chi^2 > 10^4$; $P < 0.00001$; 7 degrees of freedom) that the distribution of gold-labeled HA trimers was nonrandom

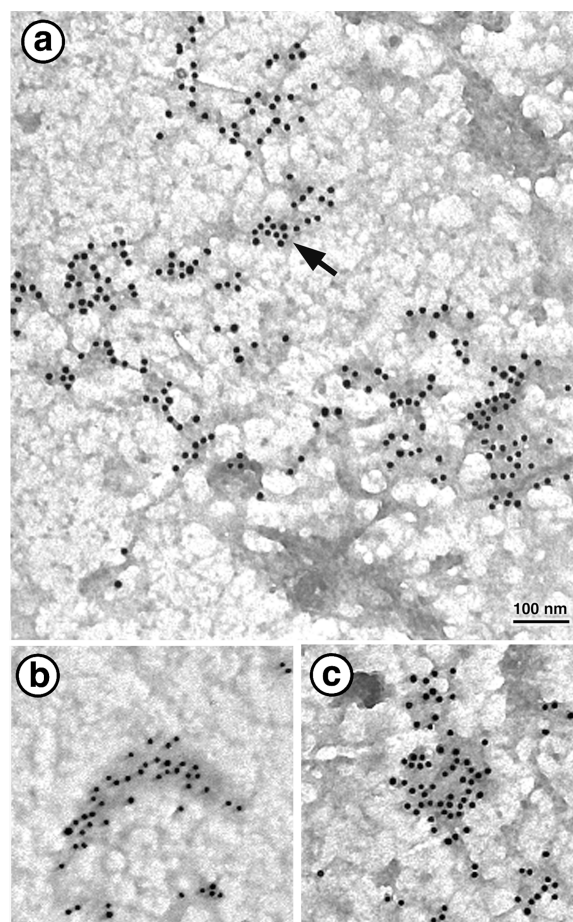
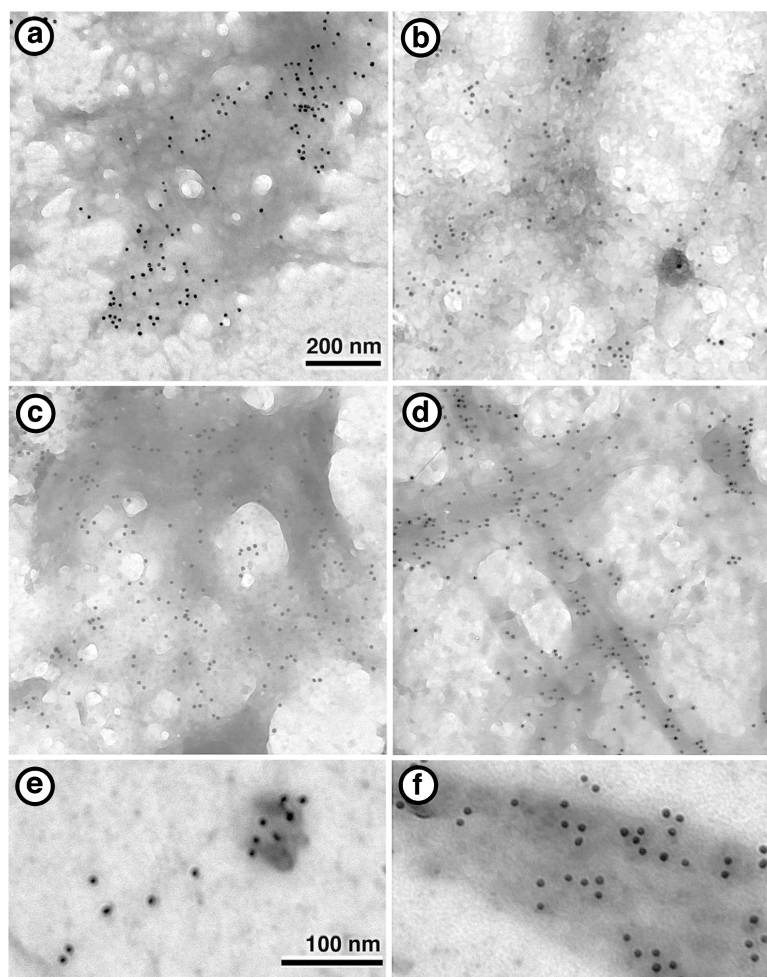


Figure 2. **En face two-dimensional view of clustered distribution of HA.** (a–c) En face view of several HAb2 fibroblast membrane sheets, fixed before labeling with α -HA mouse primary and 10-nm colloidal gold-conjugated secondary antibodies, imaged by transmission EM. Conditions were the same for a–c. Bar, 100 nm. Arrow points to an example of apparent hexagonal packing of gold.

(Fig. 4 A). As a control, identical analysis of a computer-generated random distribution of particles in a planar surface with area and overall particle density equal to those of the analyzed cellular membrane resulted in agreement between the observed and expected frequency distribution of particles per box (Fig. 4 B).

Next, the nonrandomness of the particle distribution on different spatial scales was investigated. Using the same Poisson analysis, the box size was varied from 50–350 nm and the observed frequency distribution of particles per box was fitted with Eq. 1, resulting in the χ^2 values that are shown in Fig. 4 C. The large values of χ^2 indicate a vanishing probability (p value) that the observed membrane distribution of labeled HA is consistent with the null hypothesis that HA is distributed randomly on the length scales investigated; rather, HA was distributed nonrandomly on every accessible length scale. Contrary to the result expected if partitioning into fluid domains were the cause of HA clustering, treatments with M β CD, PPMP, or PDMP, which are expected to disrupt membrane microdomains, did not result in a random distribution of HA trimers. Furthermore, the order of fixation and labeling did not affect whether the particle distribution was nonrandom on any of the length scales we investigated.

Figure 3. **Dependence of HA distribution on treatments that alter membrane lipid composition.** En face view of HAb2 cell membrane sheets (a) untreated, (b) PDMP-treated, (c) methyl- β -cyclodextrin-treated, and (d) PPMP-treated, fixed before labeling with α -HA primary antibody and 10-nm colloidal gold-conjugated secondary antibody. Bar (a–d), 200 nm. (e and f) Untreated membranes labeled with different lot of α -HA primary antibody and 6-nm colloidal gold-conjugated secondary. Bar (e and f), 100 nm.



Distribution of distances between all pairs of HA trimers

To further examine the particle distribution for characteristic cluster size and inter-cluster distance, we calculated the frequency histogram of distances, $H(r)$, between each labeled HA and every other, as a function of treatment (Fig. 5 A), where r denotes distance between gold particles. The comparison of $H(r)$ for a random distribution and the observed $H(r)$ for all treatments reveals differences: HA–HA distances less than $\sim 1.3 \mu\text{m}$ were observed more frequently than expected for a random distribution, whereas distances longer than $\sim 1.3 \mu\text{m}$ were less frequent than expected. The measured (m) frequency of HA–HA distances between ~ 0.5 and $0.9 \mu\text{m}$ was significantly higher than expected (simulated, s) for a random distribution; this increase is due to the clustered distribution of HA and likely corresponds to distances between trimers within clusters. This increase is expected to occur in a clustered HA distribution because (compared with a random distribution) HAs within a cluster will have relatively more neighbors that are closer to each other and fewer that are far away, at least on length scales near the cluster size. Hence the length scales where the observed $H(r)$ is larger than expected (0.5 – $0.9 \mu\text{m}$) give one estimate of cluster size.

Ripley's K-test

The Ripley's K-test provides a quantitative measure of the deviation of the observed HA distribution from a random distribution, as a function of the length scale examined. To further test the spatial HA distribution for characteristic cluster sizes, the modified Ripley's K-test (Eq. 2) was performed on the gold particle coordinates as a function of treatment. Fig. 5 B shows Ripley's K-test metric ($L(r) - r$) for position data from 9 to 14 images of untreated and treated membrane sheets. Note a range of consistently positive values for $L(r) - r$ that are significantly larger than the 99% confidence level (CI_{99}) (data are normalized such that the CI_{99} is equal to unity) over most length scales accessible to our analysis, indicating clustering. Note also that the K-test statistic appears to increase monotonically over the range of length scales considered ($< 700 \text{ nm}$), again indicating there was no single, well-defined size of an HA cluster.

The average $L(r) - r$ for untreated images and M β CD-, PPMP-, and PDMP-treated images (Fig. 5 B) show significant decreases in the K-test amplitude (a measure of the degree of clustering) after treatment. However, the amplitude was not reduced below the CI_{99} in any case. Thus, clusters were partially disrupted but not abolished by the lipid treatments. Furthermore, the effects of PPMP, PDMP, and M β CD on clustering appear to be similar, despite the numerous postulated side-effects of these drugs.

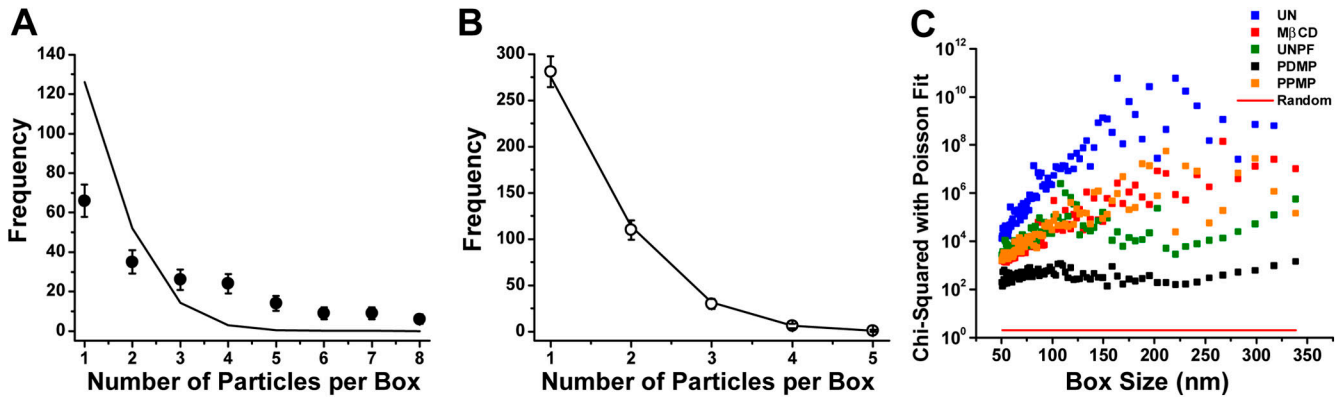


Figure 4. **Poisson analysis is inconsistent with a random membrane distribution of immunogold-labeled influenza HA trimers, as observed in en face HAb2 membrane sheets by EM.** (A) The observed frequency distribution (filled circles \pm SD) of the number of gold particles per \sim 130-nm square box within a grid superimposed on the en face image of a membrane sheet. The observed distribution is poorly described [$\chi^2 \sim 10^4$; $P < 0.00001$; $d = 7$] by a Poisson distribution (line) with the same number of particles per box and same total area under the distribution, indicating that a random membrane distribution is inconsistent with the observed distribution. Note the drastically higher than expected frequency of boxes with a large number of particles. (B) A simulated random distribution of the same number of particles within an area of the same length and width was well described by a Poisson distribution ($\chi^2 \sim 2.5$; $P \sim 0.52$; $d = 3$), which is expected. (C) The Poisson distribution does not describe the observed distribution over a wide range of length scales: the χ^2 value was large enough to reject the possibility of a random distribution of gold particles for all box sizes tested (i.e., ≥ 50 nm) and for all membrane treatments.

Nearest neighbor distance distribution

The frequency distribution of nearest neighbor distances, $N(r)$, provides a measure of the shortest distance between a labeled HA trimer and any other, and thus reports on the intra-cluster environment as a function of the various membrane treatments (Fig. 6 A). The observed $N(r)$ has a maximum, indicating a most common nearest neighbor distance, ρ_{nn} , that depends on treatment, as shown in Table I.

However, changes in $N(r)$ upon treatment were described completely by a reduced antibody binding probability or capture ratio (κ) for the treated membranes, which is also consistent with the reduced average density of gold particles upon treatment. The fraction of clustering (f_{clust}) that gave the best fit between simulation and the observed $N(r)$ was for all treatments in the range 80–100%, whereas the best-fit capture ratio κ changed more significantly, ranging from 5–7% for untreated membranes and fitting best with $\kappa \sim 2\%$ for treated membranes. Attempting to force the model to describe the observed $N(r)$ with a fixed κ by instead using f_{clust} and minimum distance between trimers as free parameters was unsuccessful, resulting in significantly larger values for the goodness of fit test (Eq. S4, available at <http://www.jcb.org/cgi/content/full/jcb.200412058/DC1>; unpublished data). Fluorescence measurements of primary antibody binding to HAb2 cells under the same conditions using the same antibody (except for the presence of fluorophores) did not show a significant difference in binding as a function of membrane treatment (unpublished data). Furthermore, the capture ratio was not significantly improved by immunolabeling with 6-nm gold-conjugated antibody (Fig. 3, E and F). These results are again consistent with only minor effects of lipid treatments on the clustering of HA on the length scales accessible in these experiments (20–900 nm).

If the labeled HA molecules are clustered with a characteristic nearest neighbor distance within the membranes we imaged, the nearest neighbor distance should not depend on the

density of labeled HA molecules. Fig. 6 B shows the most probable nearest neighbor distance ρ_{nn} in a given image field, as a function of the average labeled HA density in that field. The best-fit slope of ρ_{nn} vs. density was zero within uncertainty in all cases, except possibly PDMP treatment, where the best-fit slope was $1.3 \pm 0.7 \times 10^{-4} \mu\text{m}^3$. The independence of ρ_{nn} on HA density is strong evidence for the clustering of HA in HAb2 cell membranes.

Angular distribution of two nearest neighbors

Next, we examined the question of whether the clustering of HA in the membrane would result in angular biases of the two neighbors nearest to a given HA trimer. In particular, fluid membrane domains would be expected to have uniform density within a domain and relatively little orientational or radial order, whereas a highly packed domain with hexatic or possibly quasi-crystalline properties would be expected to show a highly biased distribution of angles, $A(\theta)$. Between a given particle (at point P) and its two nearest neighbors (say at O and Q), the angle θ is defined as the angle between the lines OP and PQ. In fact, the HA distribution in the electron micrographs occasionally showed clear examples of triangular or hexagonal packing of the gold particles at nearest neighbor distances larger than the gold particles themselves (Fig. 2). The observed $A(\theta)$ for untreated membranes and M β CD-treated membranes were plotted with control $A(\theta)$ from a simulated random distribution of the same particle density within the same area (Fig. 7). The uncertainty $\pm \sigma_A$ in the frequency A was estimated as $\sigma_A \sim \sqrt{A}$. The difference between the observed and expected $A(\theta)$ was significant: 207 ± 49 and 130 ± 30 more particles than expected were observed to have nearest neighbor angles of $< 90^\circ$ in untreated and M β CD-treated membranes, respectively, indicating that these biases are significant, independent of membrane cholesterol content.

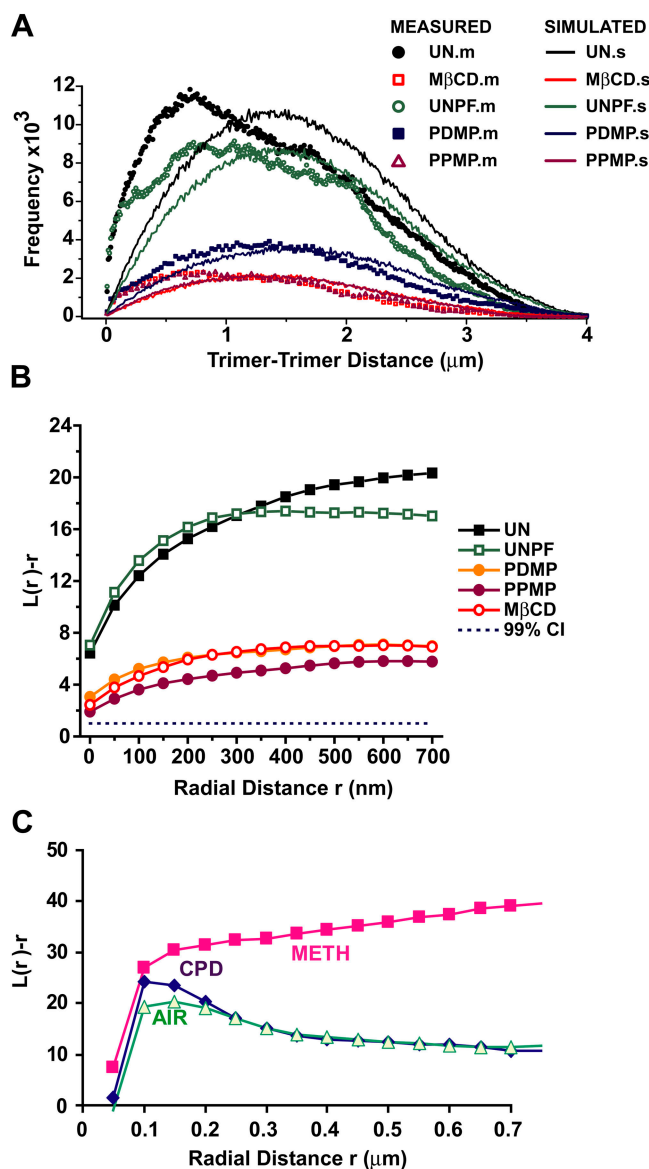


Figure 5. Pair-distance frequency distribution and K-test reveal evidence for lipid-dependent clustering of influenza HA on many length scales. (A) The measured (.m) frequency distribution (points) of all distances between labeled HA trimers in en face HAb2 membrane sheets is compared against that for a simulated (.s) random distribution of particles (solid lines). (UN) Untreated, labeled then fixed. (UN-PF) Untreated membrane, fixed then labeled. (MβCD) Methyl-β-cyclodextrin treated, fixed then labeled. (PPMP) PPMP treated, fixed then labeled. (PDMP) PDMP treated, fixed then labeled. Note that the random distribution does not describe the observed HA distribution, and that the observed frequency of distances less than ~900 nm is significantly higher than expected, indicating clustering on submicron length scales. (B) Ripley's K-test metric $L(r) - r$ is plotted as a function of inter-particle distance r for selected analyzed electron micrographs (same treatment key as in A) with 99% confidence interval (dotted line). Note strong positive values of $L(r) - r$, indicating clustering on all accessible length scales (shown here up to 700 nm). The magnitude of $L(r) - r$ decreases significantly upon membrane treatments, indicating that the degree of clustering may be reduced, but that clustering is not abolished by the treatments. (C) Ripley's K-test metric $L(r) - r$ for untreated, air dried (AIR), critical point dried (CPD) and air dried on methylcellulose (METH) shows that clustering does not depend on whether samples were dried in air. The significantly larger $L(r) - r$ values under methylcellulose indicates that the methylcellulose may have had some effect on the pattern of clustering.

Fluorescence resonance energy transfer

We have used fluorescence resonance energy transfer (FRET) to probe the lipid dependence of the HA distribution on molecular length scales. Cy3- and Cy5-labeled α -HA mAbs were used as a FRET pair with nominal $r_0 \sim 5.3$ nm (Ishii et al., 1999). The FRET efficiency was measured by donor dequenching upon acceptor photobleaching in fixed HAb2 cells as a function of lipid treatments (applied before fixation) and antibody concentration. Fig. 8 shows the measured FRET in untreated cells and cells treated with MβCD, PDMP, and PPMP. Significant decreases in FRET occurred upon all lipid treatments and at all antibody concentrations. Measurements made on two different microscopes (confocal and widefield) are presented and show similar effects. Monte-Carlo modeling of the expected FRET efficiency for a clustered distribution of HA trimers (see supplemental material for details; available at <http://www.jcb.org/cgi/content/full/jcb.200412058/DC1>) describes the observed FRET efficiency (Fig. 8), whereas FRET from a simulated random distribution did not describe the measured FRET as well. The strong dependence of the FRET efficiency on treatments that altered membrane lipid composition indicates that relative distance and orientation of HA trimers is being altered on the molecular length scales (6–7 nm) by such treatments. This corroborates the findings of Henis and colleagues using FRAP that show HA diffusion changes with cholesterol depletion (Shvartsman et al., 2003). Our results are a complement to the EM results, which indicate relatively small effects of treatments on the HA distribution on longer (≥ 20 nm) length scales.

Discussion

We have shown that the two-dimensional distribution of influenza HA is highly nonrandom in fibroblast plasma membranes on all accessible length scales, from 6 nm to 900 nm. Nearest neighbor distance was independent of HA density over a wide range. FRET, which measures clustering on length scales < 10 nm, showed that the shortest distances between trimers were increased by agents that remove cholesterol and inhibitors of glycosphingolipid synthesis. The amount of FRET was too high for a random distribution and the density dependence is weaker than expected for random. These results are inconsistent with the hypothesis that clustering results from proteins partitioning into preexisting, fluid-ordered raft domains, wherein they have a random distribution. The results are consistent with the idea that specific proteins and lipids self-assemble in the plane of the membrane to form nonrandom microscopic or nanoscopic domains.

Two-dimensional analysis of HA distribution: comparison with related methods and raft markers

The analysis presented here using a number of methods shows decisively that HA is clustered in the plasma membrane of HAb2 cells, consistent with previous results (Takeda et al., 2003). Our results analyze a large number of gold particles, providing improved statistics, and to our knowledge provide for the first time the two-dimensional distribution of HA within

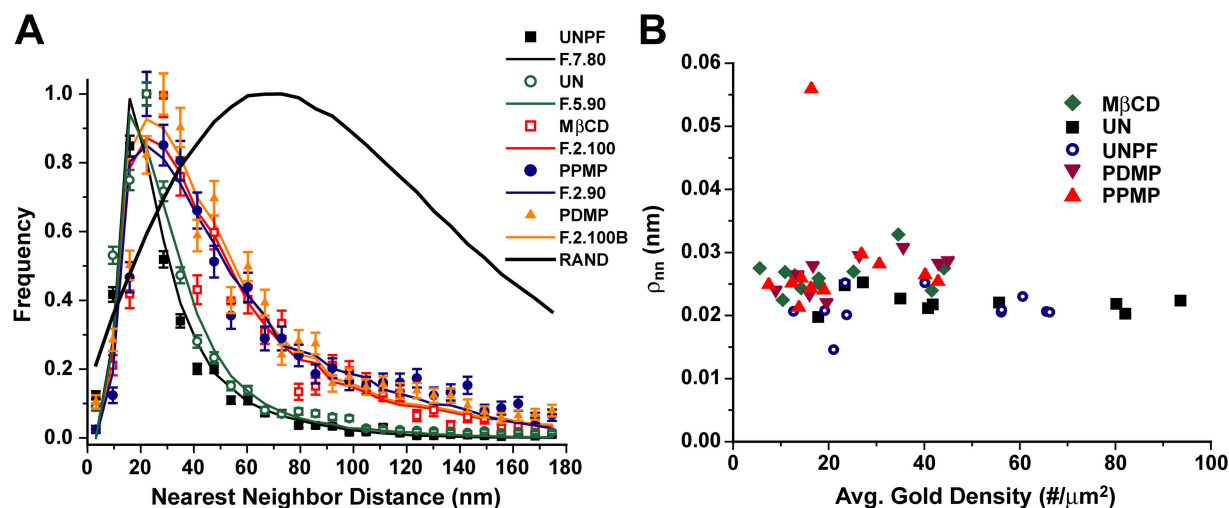


Figure 6. Effect of treatments on the observed nearest neighbor distance distribution (points) can be explained by changes in antibody binding efficiency, or capture ratio, κ . (A) The frequency distribution of nearest neighbor distances $N(r)$ between 10-nm immunogold-labeled HA trimers on HA2B cell membrane sheets shows a maximum value from 25–30 nm with little dependence on treatment and fixation. Samples were fixed and then labeled unless noted otherwise. The observed distributions were least-squares fitted with Monte-Carlo simulations (solid lines) of clustered distributions of HA trimers (see Materials and methods) that were least-squares fitted to the observed $N(r)$ as a function of capture ratio (κ) and fraction of clustered trimers (f_{clust}). Best fit between observed and simulation occurred in untreated membranes (black squares) for $\kappa = 7\%$, $f_{\text{clust}} = 80\%$ (black line), in untreated membranes labeled before fixation (open green circles) for $\kappa = 5\%$, $f_{\text{clust}} = 90\%$ (green line), in MβCD-treated membranes (open red squares) for $\kappa = 2\%$, $f_{\text{clust}} = 100\%$ (red line), in PPMP-treated membranes (black circles) for $\kappa = 2\%$, $f_{\text{clust}} = 90\%$, and in PDMP-treated membranes (orange triangles) for $\kappa = 2\%$, $f_{\text{clust}} = 100\%$ (orange line). Nearest neighbor histogram expected for a random distribution is shown for comparison (RAND; black line). (B) Peak nearest neighbor distance ρ_{nn} does not depend strongly on the average gold density per square micron, strong evidence for a clustered membrane distribution of HA, independent of treatment.

the plane of the membrane. Takeda et al. (2003) analyze in one linear dimension 363 gold particles labeling wild-type trimeric HA and 1,298 gold particles labeling nonraft mutant trimeric HA; we analyze in two dimensions 8,245 gold particles labeling trimeric HA in untreated membranes, 1,988 in MβCD-treated membranes, 2,585 in PDMP-treated membranes, and 2,198 in PPMP-treated membranes.

A second significant observation apparent from the images in Figs. 1–3 is the colocalization of the HA with electron-dense membrane regions, which bears some similarity in appearance to the colocalization of immunogold-labeled FcεRI and IgE–FcεRI complexes with osmiophilic membrane regions reported previously (Wilson et al., 2000, 2002). More work is needed to interpret this finding.

Our results, which show clustering on many length scales, are in contrast to the findings of Prior et al. (2003) for the protein Ras, whose clusters are apparently less extended and thus have a much better defined distribution of sizes. Such differences likely relate in part to the relative strength of specific protein–lipid and protein–protein interactions within the plane of the membrane, which may derive from differences in modes of attachment to the membrane.

Treatments altering lipid composition minimally change observed HA distribution

The effect of cholesterol removal and glycosphingolipid synthesis inhibition on the degree and size of clusters was surprisingly minor: based on the K-test (Fig. 5), clusters were somewhat broken up, but they were not abolished. A Kolmogorov–Smirnov test using area-normalized $L(r) - r$ for untreated and MβCD-treated

membranes resulted in a significant difference between the two distributions ($P < 10^{-6}$). The Poisson analysis (Fig. 4 C) of number of particles per box also shows a highly nonrandom distribution of labeled HA after each of the three treatments. These results indicate that clusters are only partially disrupted by the treatments. On the other hand, MβCD treatment reduces the probability of FRET (sensitive to length scales of ~ 3 –9 nm) between antibody-labeled HA trimers (Fig. 8), consistent with lipid-dependent disruption of HA packing at molecular length scales. Perhaps the large-scale clusters depend more on cytoskeletal interactions.

One well-established example of protein–protein interactions that results in membrane structures of a similar size is the clathrin-coated pit (Mahaffey et al., 1989). However, our EM results do not show gold-labeled HA in any of the features of clathrin-coated pits observed by similar methods (Mahaffey et al., 1989; Lin et al., 1991), and this may correlate with the relative stability of HA on the surface of the cell membrane (Roth et al., 1986). Membrane domains such as caveolae could also be highly relevant to the internalization dynamics of HA.

Table 1. Summary of nearest neighbor distances and gold density vs. membrane treatment

Treatment	Peak nearest neighbor distance (nm ± SD)	Average nearest neighbor distance (nm ± SD)	Average gold density (#/μm ² ± SD)
UN-PF	17.0 ± 0.5	48 ± 5	65 ± 34
UN	18.5 ± 0.6	46 ± 5	82 ± 46
MβCD	24.8 ± 0.5	77 ± 10	31 ± 21
PPMP	28.1 ± 0.5	75 ± 7	33 ± 18
PDMP	28.7 ± 0.7	71 ± 5	41 ± 20

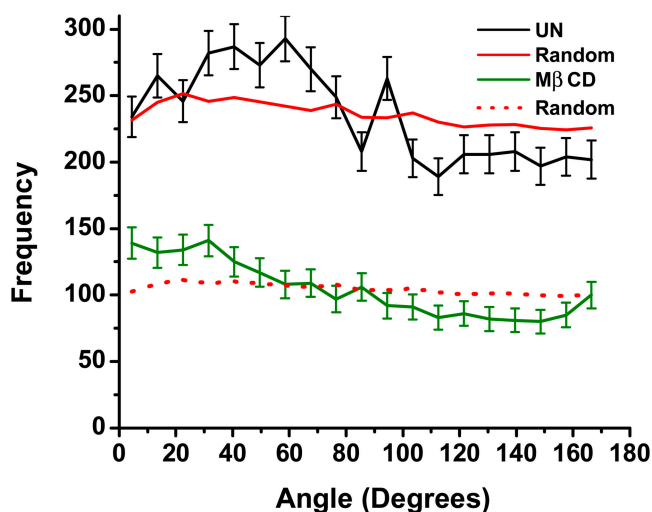


Figure 7. Biases in the distribution of angles between a given HA molecule and its two nearest neighbors. Certain angles $<90^\circ$ are observed more frequently than expected for untreated (UN) and methyl- β -cyclodextrin-treated (M β CD) HA₂ membrane sheets, compared with the expected frequency for a simulated random distribution (solid lines) of an equal number and density of HA trimers on a planar surface. Differences between angular histograms in untreated and M β CD-treated membranes could be explained by the same changes in capture ratio that resulted from fitting the nearest neighbor histogram with simulation (not depicted).

Packing of HA trimers with neighbors

The significant biases in the angular distribution of nearest neighbor HA demonstrates that trimers are ordered in their orientation relative to one another. Because most of the nearest neighbor distances (~ 20 – 30 nm) are two- to three-fold larger than the gold size (~ 10 nm), it is unlikely that steric hindrance between gold particles determines ordering. Furthermore, no significant orientational biases were observed in a two-dimensional simulation of circular particles with similar size and density per unit area. Systems with long-range interparticle interactions stronger than those of fluids are known to form phases (termed “hexatic”) intermediate between crystalline and fluid (Li et al., 1996). Thus, although the miscible fluid phase domain model is inconsistent with our observations, the actual phase of HA domains in biological membranes may be intermediate between fluid and solid (i.e., more ordered than liquid ordered but less ordered than gel). For example, there may be condensed phases of cholesterol and sphingomyelin surrounding the transmembrane domain of the HA trimer (Radhakrishnan and McConnell, 1999). Such a phase does retain some important features of solid phase domains (such as orientational biases) and may exhibit others such as lattice positions, while retaining the apparently biologically crucial property of fluid phases: lateral mobility. However, these results are also consistent with other models. Interactions with caveolae could result in ordering on 10^{-8} to 10^{-7} m length scales while other mechanisms might be necessary to explain ordering on longer length scales. Strong interactions between membrane constituents and the cytoskeleton, for example, could result in lattice-like arrangements of membrane proteins on nanometer length scales.

Models for lipid domains

HA clustering on many length scales.

Our results show clustering of HA on many length scales. A central finding of an important review of membrane microdomain models (Anderson and Jacobson, 2002) is that different methods yield different sizes for rafts. Our results suggest that for proteins such as HA, clustering will be observed on the length scales accessible to a method. Should a method only be able to access a narrower range of length scales than does the protein, one may erroneously conclude that this narrow range defines the size distribution of the cluster. A similar situation occurs in the measurement of the distribution of fusion pore conductances (Zimmerberg, 1993). Measurement of cluster size by different methods may result in different sizes for the same clusters. This is the situation today in the field of lipid rafts, which finds no consensus on domain size but a plethora of models. Second, the presence of nonrandomness on nearly all observed length scales precludes the possibility of a uniform distribution within domains, except on length scales we do not have access to (<6 nm, which is 2 nm less than the diameter of the smallest cylinder that could enclose the HA trimer ectodomain). Despite nonrandomness on all accessible length scales, clusters may occur preferentially over a certain range of length scales. Indeed, we find a peak in the pair-distance distribution (Fig. 5) and discuss this below in terms of the size of the viral envelope. In fact, we think that one important achievement of this work is to avoid any arbitrary definitions of domains that would be necessary to obtain a size distribution of clusters. Thus, our statement on the nonrandom nature of the distribution at all length scales is model independent. Some raft models of membrane domains propose that proteins partition preferentially into fluid phase (liquid ordered) lipid domains wherein proteins are miscible and lateral diffusion is unrestricted. Such models that would predict a random distribution within such a domain are inconsistent with our observations. However, it is possible that HA does partition into preexisting domains, but is immiscible in the lipid environment of that domain. In that case, the HA would aggregate to minimize its exposure to the domain lipids. Finally, as stated above, in a partitioning system one would expect a dependence of the peak nearest neighbor distance on density, and in our system the observed dependence is insignificant.

Density independence of HA nearest neighbor distance. Although the finding that local HA density within domains is constant is inconsistent with a miscible partitioning model, this feature is not unique to HA clusters. Density independence of the homoFRET characterizing GPI-linked proteins is also not explained by a miscible partitioning model (Sharma et al., 2004). Again, condensed phases of cholesterol and sphingolipids have been proposed to explain this phenomenon (Sharma et al., 2004). It may be useful to divide the universe of raft models into those that feature partitioning into preexisting domains, and self-assembly of proteins and lipids into specific biological structures.

Significance for viral assembly and fusion

It is clear that cellular lipids have the propensity to form coexistence regions of liquid-ordered and liquid-disordered phases,

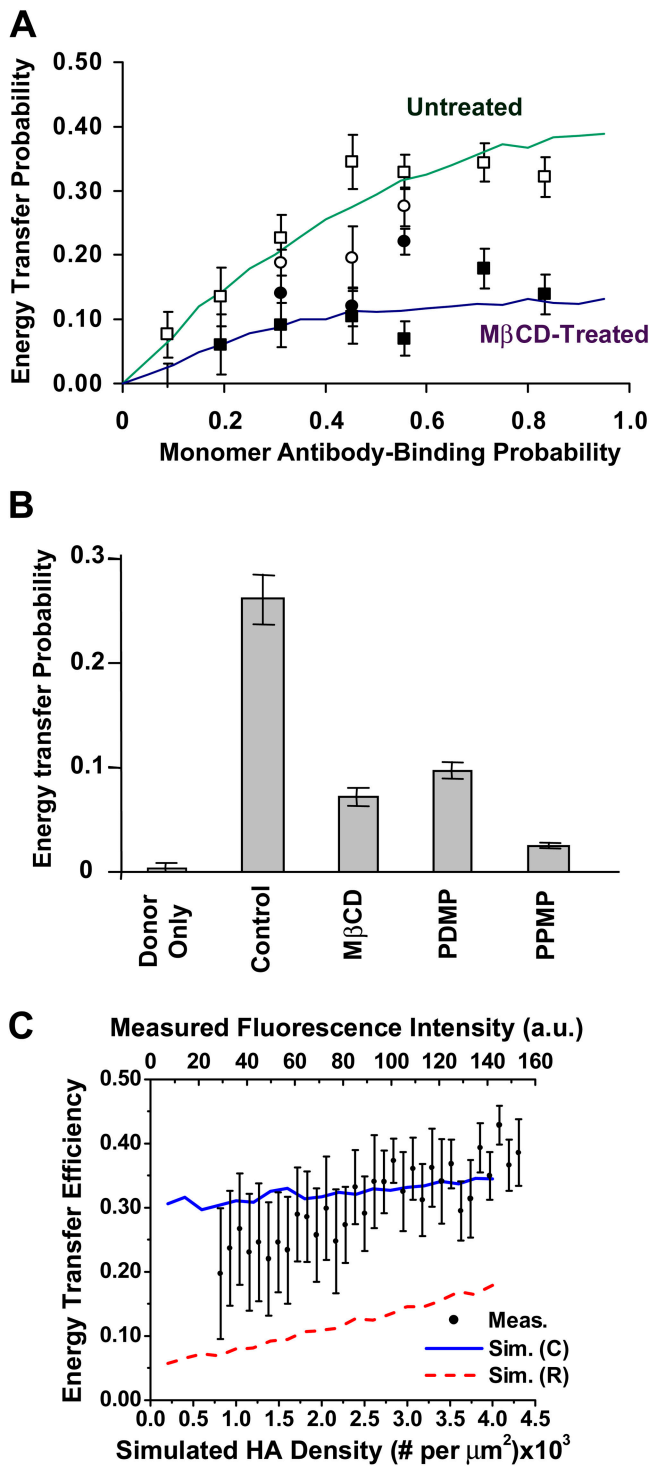


Figure 8. Lipid-dependent FRET between Cy3- and Cy5-labeled antibody against HA in HAB2 cells fixed before labeling reflects changes in HA distribution or orientation on molecular (~ 6 nm) length scales. (A) The energy transfer probability measured in a widefield fluorescence microscope (squares) and confocal microscope (circles) by acceptor photobleaching shows a significant decrease in cells treated with M β CD (filled points) for 30 min before fixation compared with cells that were untreated before fixation (open points). FRET was measured as a function of antibody dilution, from which the antibody binding probability is calculated using the measured antibody K_d . Monte-Carlo simulations of FRET efficiency for a clustered (solid green line) and unclustered (solid blue line) HA distribution describe the measured efficiency and are consistent with partial disruption of HA clustering on molecular length scales by lipid treatments. (B) Energy transfer probability as a function of lipid treatments at fixed antibody

as revealed by macroscopic domain formation in phospholipid bilayers formed from lipid mixtures (Korlach et al., 1999; Feigenson and Buboltz, 2001; Veatch and Keller, 2002, 2003; Baumgart et al., 2003). Given the ability of cell membrane lipids to self-organize discrete domains, it is compelling to suggest that domains are used by cells to organize the plasma membrane (Simons and Ikonen, 1997).

The link between membrane microdomain association, clustering, and biological function merits further investigation. Some studies find no effect of M β CD on cell–cell fusion mediated by HA (Melikyan et al., 1999; Armstrong et al., 2000). The finding that viral infectivity is dependent on membrane cholesterol content (Takeda et al., 2003) is consistent with our observations that membrane fusion catalyzed by the major envelope protein of influenza, HA, is M β CD sensitive (unpublished data), but this may reflect nonraft aspects of cholesterol action because VSV is also inhibited by M β CD (Takeda et al., 2003). Our results here, together with electron microscopic data on viral–liposome fusion (Kanaseki et al., 1997) and our previous work on membrane fusion (Chernomordik et al., 1998; Frolov et al., 2000), are consistent with (but not proof of) the formation of a fusion “rosette,” where a high local concentration of HA, cholesterol, and sphingolipids may be the crucial quantity for membrane fusion (Markovic et al., 2001). Disruption of this local molecular ordering by removal of cholesterol is consistent with fluorescence mobility measurements that generally show an increase in mobility of raft-associated membrane proteins such as HA when membrane cholesterol is depleted (Shvartsman et al., 2003). Lipid-dependent trimer–trimer interactions may be more relevant to fusion activity and may likewise control clustering on the length scale of individual trimers (~ 8 nm).

With respect to domain size distribution and viral budding sites, the frequency distribution $H(r)$ of distances between HA molecules was clearly nonrandom, with various maxima and minima indicating that certain intermolecular distances were favored (see Fig. 5). The combined distributions for all images with the same treatment each showed some bias toward 0.5–0.9 μm , irrespective of treatment. These distances can be interpreted as a characteristic size of clusters (Vereb et al., 2000), but because HA clusters span many size scales we view this interpretation with caution. Such a cluster size is potentially consistent with the use of microdomains as viral budding sites, as suggested previously for clusters of HA in cells infected with influenza virus (Takeda et al., 2003) and vesicular stomatitis virus (Brown and Lyles, 2003). It seems larger than the usually given size of a single influenza virus (~ 0.1 – 0.2 μm), but there is heterogeneity in the size and shape distribution of the influenza virus (Ruigrok et al., 1985). If the entire

concentration shows significant reduction in FRET efficiency in M β CD-, PDMP-, and PPMP-treated membranes compared with untreated membranes, suggesting that whereas lipid-dependent redistribution of HA trimers on long length scales (>20 nm) appears to be minor, that significant redistribution occurs on molecular (~ 6 nm) length scales. (C) Measured energy transfer probability (Meas.) vs. fluorescence intensity (arbitrary units) agrees more closely with the simulated energy transfer vs. HA density for a clustered HA distribution (Sim. C) than with a random distribution (Sim. R).

domain buds out with the capsid, then cylindrical or other irregular viral shapes could be understood in terms of the heterogeneity in the domains seen here. Allowing deviations from a circular shape, such predictions are consistent with our observations, although we also observe clustering on many other length scales.

Summary

We present the first quantification of the two-dimensional distribution of influenza HA trimers expressed on fibroblast cell surfaces spanning a nearly 30-fold range of average density. Our electron micrographs and the accompanying analysis reveal HA clustering on many length scales. These results are in contrast to the expected observation that HA would be found in domains of a well-defined size (as predicted for other proteins by various raft models). Instead, clusters are observed to have sizes ranging across all accessible (reliably observable) length scales. Furthermore, the density within domains is nonuniform, indicating that partitioning with ideal mixing of HA does not describe the process that distributes HA laterally in the membrane, at least within accessible length scales.

Our results are consistent with models invoking specific protein–lipid and protein–protein interactions that assemble membrane domains, such as the lipid shell model, as well as models of aggregation of extremely small rafts. Indeed, within the context of the lipid shell model, these clusters of HA may represent larger-scale biological structures into which HA and shell lipids have coalesced. In other words, the molecular features of the HA trimer have presumably evolved to allow self-assembly in the cell membrane of a cluster of lipids and proteins needed for successful continuity of the viral life cycle, namely budding and fusion. We can term this structure the viral “pre-envelope” to distinguish it from the nascent envelope that forms at the budding site upon interaction with other viral components. The observed lipid-dependent differences in clustering at long and short length scales imply that different forces may be acting to induce order at the molecular (FRET) level and at the microscopic (EM) level. The presence of order on such a wide range of length scales may answer the question of why different experimental methods with specific ranges of accessible length scales observe different sizes for rafts.

Materials and methods

Cell culture, fixation, and immunogold labeling

Fibroblasts expressing the Japan strain of HA₀, here referred to as HA, (HAb2 cells), were grown as a monolayer on glass coverslips (22-mm square) to 80% confluence. The growth medium was washed with PBS (w/Ca²⁺, Mg²⁺) at RT (~23°C), twice. The cells were washed twice in 0.1 M Hendry's phosphate buffer (HPB; see supplemental material), then fixed in 2% PFA and 0.05% glutaraldehyde (followed eventually by 4% glutaraldehyde; please see supplemental material for further details), then labeled with anti-HA mAb, followed by gold-conjugated secondary antibody.

Membrane retrieval and preparation for EM

After gold labeling, whole membrane segments were retrieved according to the procedure adapted from Sanan and Anderson (1991), with minor modifications.

Cell preparation for thin sectioning

Cells for thin sectioning were grown, fixed, and immunostained according to the above protocol, then prepared for EM essentially as described by

Neale and colleagues (Fernando et al., 1989), with minor modifications. Ultrathin and serial cross sections (50-nm thick) were cut.

Imaging

En face and serial sections were imaged using a transmission electron microscope (100 CX; JEOL) at 50,000× and 80 kV.

Image analysis

Horizontal and vertical coordinates of gold particles were recorded from the images manually using NIH ImageJ. Coordinate assignments assumed the imaged membrane to be a planar surface with negligible height variation out of plane. Membrane serial sections of HAb2 cells expressing HA constitutively indicate that out-of-plane invaginations and buds had heights of up to 100 nm over lateral distances of several micrometers. The en face membrane preparation method brings the sample through the air–water interface and results in considerable flattening of the membranes as revealed by tomographic reconstruction.

Membrane treatments

Before fixation and gold labeling, some cells received one of three types of treatment: (1) methyl-β-cyclodextrin (MβCD), which removes cholesterol from membranes (Klein et al., 1995; Niu et al., 2002), incubated with cells in PBS at final concentration 10 mM for 30 min at 4°C; (2) glucosylceramide synthase inhibitor PDMP; or (3) glucosylceramide synthase inhibitor PPMP (Abe et al., 1992) (Matreya, Inc.). PDMP and PPMP were incubated with cells in Dulbecco's minimum essential medium at a final concentration of 10 μM for 48 h at 37°C. These cells were then processed to produce either membrane sheets or material for thin sections.

Numerical image analysis

(1) Poisson analysis of clustering. The field of each image was divided uniformly into square areas (boxes) and the particles in each box were counted. The frequency distribution of the number of particles per box was then fit using a Poisson distribution:

$$P(x,n) = \frac{A_0 e^{-x} x^n}{n!} \quad (1)$$

where x is the mean of the frequency distribution (the mean number of particles per box), n is the number of particles per box, and A_0 is a constant. The number of degrees of freedom was determined from the histogram, taking into account the number of bins within the histogram that had a count of 6 or higher; bins with fewer than five counts were not used for determination of the χ^2 value.

(2) Pair-distance frequency distribution. The distribution of distances between each labeled HA particle and all other labeled HA particles was calculated for each image and binned by 5 nm into a histogram. The distribution for a random field of particles with the same density per unit area and same total area was calculated and compared with the experimental distribution.

(3) K-test for clustering. The Ripley's K-test (Ripley, 1977, 1979; Prior et al., 2003) was performed, which measures the number of particles within a given radius r of any given labeled HA molecule as follows:

$$L(r) - r = \sqrt{N(r)/\pi D} - r \quad (2)$$

where $N(r)$ is the number of particles within a distance r of a given particle, and D is the average particle density per unit area. Positive values of $L(r)$ indicate clustering on length scale r .

(4) Nearest neighbor distance distribution. The frequency distribution of nearest neighbor distances $N(r)$ between labeled HA molecules was calculated using a fixed bin size of either 1 nm or 6.35 nm, then compared with results for a random or simulated clustered field of particles at the same density per unit area and the same total area. Replicate experiments (various images of membranes given the same treatment) were summed to yield a global histogram.

(5) Angular neighbor distribution. The angle between a given trimer (as the vertex of the angle) and its two nearest neighbors was calculated for all trimers within each image. A global histogram $A(\theta)$ as a function of the angle θ was generated from the sum of the histograms for each image with a given membrane treatment.

(6) Colocalization of HA trimers with electron-dense membrane patches. Images were scanned from negatives at high resolution and read into custom software that identifies gold particles and dark membrane regions. Gold particles were located by scanning the image in a raster pat-

tern and finding all points with intensity darker (pixel value lower) than a fixed threshold. For each identified gold particle, the average pixel intensity as a function of radius r from the center of the particle was calculated, averaged for all images with the same treatment, and fitted to the function $A + Be^{-r/r_0}$ to obtain a characteristic length scale (r_0) over which the gold particles and electron-dense membrane regions were correlated.

FRET microscopy

FRET microscopy was performed essentially as described in Kenworthy and Edidin (1999). Anti-HA mAb FC125 was conjugated with succinimidyl ester derivatives of Cy3 or Cy5 (Amersham Biosciences) as indicated by the manufacturer, to an average level of ~ 2 fluorophores per IgG molecule. HAB2 (untreated or cholesterol/SM/GSL depleted) cells were grown on 4-well coverglass chambers (#1.5; Nalge Nunc), fixed in 4% PFA at RT for 20 min followed by labeling with a mixture of Cy3- or Cy5-conjugated mAb (50 $\mu\text{g}/\text{ml}$ concentration) and imaged directly.

Digital images were collected using a 20 \times , 0.75 NA objective on a microscope (Diaphot 300; Nikon) using a 12-bit scientific CD camera (model CH250; Photometrics). Fluorescence was excited with a xenon arc lamp and visualized using Cy3 and Cy5 filter sets (Chroma Technology Corp.). Images of Cy3 and Cy5 before (Cy3pre and Cy5pre) and after (Cy3post and Cy5post) bleaching the Cy5 were collected using identical exposure times, typically 10 s. Cy5 was >95% photobleached by continuously exciting it for 7–8 min. Custom-designed software (available upon request) was used to analyze the FRET data. This program tabulates the average fluorescence intensity from identical regions of interest from each of the four images in each sample after background subtraction. Energy transfer probabilities were then calculated as their efficiencies (E) from the background-corrected values of Cy3 fluorescence as

$$E_{\text{exp}} = [F_{\text{cy3}}^{\text{post}} - F_{\text{cy3}}^{\text{pre}}] / F_{\text{cy3}}^{\text{post}} \quad (3)$$

where $F_{\text{cy3}}^{\text{pre}}$ and $F_{\text{cy3}}^{\text{post}}$ are the measured fluorescence Cy3 intensities before and after acceptor photobleaching. Typically data were collected from 4–5 fields of cells for each treatment. For further analysis, data were pooled by treatment and the average energy transfer efficiency compared across treatments. The average fluorescence intensity of the acceptor was also monitored, to confirm that the average surface densities of labeled HA molecules were constant across treatments.

Online supplemental material

Online material includes further details of cell culture and sample preparation for immunogold EM, numerical modeling of the FRET efficiency as a function of experimental parameters, and details on methods of analysis of protein distributions: Poisson, and Ripley's K-test. Next are descriptions of methods for Monte-Carlo simulation of membrane HA and immunogold distributions and fitting of the observed distributions using results from the simulations, followed by estimates of the range of accessible length scales in these experiments. Finally, we discuss possible artifacts due to antibody labeling, fixation, sample drying, and projection of gold particle positions from three dimensions into a two-dimensional plane. Online supplemental material available at <http://www.jcb.org/cgi/content/full/jcb.200412058/DC1>.

First and foremost, we thank Dr. Michael G. Roth for his insightful discussions, instrumental in guiding our thinking on the raft field, the place of HA in that field, and the role of the transmembrane domain of HA in its raft localization. The authors also thank Drs. Paul Blank, Thomas Reese, Yuri Chizmadzhev, and Xiaobing Chen for illuminating discussions; Dr. Gerald Feigenson for suggesting the domain immiscibility model; Dr. D. Axelrod for suggesting the fast-aggregation model; and John Hancock for suggesting that we use Diggle's edge corrections.

Submitted: 9 December 2004

Accepted: 16 May 2005

References

Abe, A., J. Inokuchi, M. Jimbo, H. Shimeno, A. Nagamatsu, J.A. Shayman, G.S. Shukla, and N.S. Radin. 1992. Improved inhibitors of glucosylceramide synthase. *J. Biochem. (Tokyo)*. 111:191–196.

Abe, A., N.S. Radin, and J.A. Shayman. 1996. Induction of glucosylceramide synthase by synthase inhibitors and ceramide. *Biochim. Biophys. Acta*. 1299:333–341.

Anderson, R.G.W., and K. Jacobson. 2002. A role for lipid shells in targeting pro-

teins to caveolae, rafts, and other lipid domains. *Science*. 296:1821–1825.

Armstrong, R.T., A.S. Kushnir, and J.M. White. 2000. The transmembrane domain of influenza hemagglutinin exhibits a stringent length requirement to support the hemifusion to fusion transition. *J. Cell Biol.* 151:425–437.

Baumgart, T., S.T. Hess, and W.W. Webb. 2003. Imaging coexisting fluid domains in biomembrane models coupling curvature and line tension. *Nature*. 425:821–824.

Bavari, S., C.M. Bosio, E. Wiegand, G. Ruthel, A.B. Will, T.W. Geisbert, M. Hevey, C. Schmaljohn, A. Schmaljohn, and M.J. Aman. 2002. Lipid raft microdomains: a gateway for compartmentalized trafficking of Ebola and Marburg viruses. *J. Exp. Med.* 195:593–602.

Brown, E.L., and D.S. Lyles. 2003. Organization of the vesicular stomatitis virus glycoprotein into membrane microdomains occurs independently of intracellular viral components. *J. Virol.* 77:3985–3992.

Bukrinskaya, A.G., J.G. Molotkovsky, E.L. Vodovozova, Y.M. Manevich, and L.D. Bergelson. 1987. The molecular organization of the influenza virus surface. Studies using photoreactive and fluorescent labeled phospholipid probes. *Biochim. Biophys. Acta*. 897:285–292.

Chen, C.S., A.G. Rosenwald, and R.E. Pagano. 1995. Ceramide as a modulator of endocytosis. *J. Biol. Chem.* 270:13291–13297.

Chernomordik, L.V., V.A. Frolov, E. Leikina, P. Bronk, and J. Zimmerberg. 1998. The pathway of membrane fusion catalyzed by influenza hemagglutinin: Restriction of lipids, hemifusion, and lipidic fusion pore formation. *J. Cell Biol.* 140:1369–1382.

Edidin, M. 2001. Shrinking patches and slippery rafts: scales of domains in the plasma membrane. *Trends Cell Biol.* 11:492–496.

Edidin, M. 2003. Lipids on the frontier: a century of cell-membrane bilayers. *Nat. Rev. Mol. Cell Biol.* 4:414–418.

Ellens, H., J. Bentz, D. Mason, F. Zhang, and J.M. White. 1990. Fusion of influenza hemagglutinin-expressing fibroblasts with glycophorin-bearing liposomes: role of hemagglutinin surface density. *Biochemistry*. 29:9697–9707.

Feigenson, G.W., and J.T. Buboltz. 2001. Ternary phase diagram of dipalmitoyl-PC/dilauroyl-PC/cholesterol: nanoscopic domain formation driven by cholesterol. *Biophys. J.* 80:2775–2788.

Fernando, N.S., N.W. Boyce, S.R. Holdsworth, and T.J. Neale. 1989. Localization of antglomerular basement membrane-binding polyclonal antibodies in rat lung and kidney using post-embedding immunogold electron microscopy. *Br. J. Exp. Pathol.* 70:557–565.

Frolov, V.A., M.S. Cho, P. Bronk, T.S. Reese, and J. Zimmerberg. 2000. Multiple local contact sites are induced by GPI-linked influenza hemagglutinin during hemifusion and flickering pore formation. *Traffic*. 1:622–630.

Fujiwara, T., K. Ritchie, H. Murakoshi, K. Jacobson, and A. Kusumi. 2002. Phospholipids undergo hop diffusion in compartmentalized cell membrane. *J. Cell Biol.* 157:1071–1081.

Hisaki, H., H. Shimasaki, N. Ueta, M. Kubota, M. Nakane, T. Nakagomi, A. Tamura, and H. Masuda. 2004. In vivo influence of ceramide accumulation induced by treatment with a glucosylceramide synthase inhibitor on ischemic neuronal cell death. *Brain Res.* 1018:73–77.

Ishii, Y., T. Yoshida, T. Funatsu, T. Wazawa, and T. Yanagida. 1999. Fluorescence resonance energy transfer between single fluorophores attached to a coiled-coil protein in aqueous solution. *Chem. Phys.* 247:163–173.

Kanaseki, T., K. Kawasaki, M. Murata, Y. Ikeuchi, and S. Ohnishi. 1997. Structural features of membrane fusion between influenza virus and liposome as revealed by quick-freezing electron microscopy. *J. Cell Biol.* 137:1041–1056.

Kenworthy, A.K., and M. Edidin. 1999. Imaging fluorescence resonance energy transfer as probe of membrane organization and molecular associations of GPI-anchored proteins. *Methods Mol. Biol.* 116:37–49.

Kenworthy, A.K., B.J. Nichols, C.L. Remmert, G.M. Hendrix, M. Kumar, J. Zimmerberg, and J. Lippincott-Schwartz. 2004. Dynamics of putative raft-associated proteins at the cell surface. *J. Cell Biol.* 165:735–746.

Kilsdonk, E.P., P.G. Yancey, G.W. Stoudt, F.W. Bangerter, W.J. Johnson, M.C. Phillips, and G.H. Rothblat. 1995. Cellular cholesterol efflux mediated by cyclodextrins. *J. Biol. Chem.* 270:17250–17256.

Klein, U., G. Gimpl, and F. Fahrenholz. 1995. Alteration of the myometrial plasma membrane cholesterol content with beta-cyclodextrin modulates the binding affinity of the oxytocin receptor. *Biochemistry*. 34:13784–13793.

Korlach, J., P. Schwille, W.W. Webb, and G.W. Feigenson. 1999. Characterization of lipid bilayer phases by confocal microscopy and fluorescence correlation spectroscopy. *Proc. Natl. Acad. Sci. USA*. 96:8461–8466.

Li, M., W.L. Johnson, and W.A. Goddard III. 1996. Evidence of hexatic phase formation in two-dimensional Lennard-Jones binary arrays. *Phys. Rev. B Condens. Matter*. 54:12067–12072.

Lin, H.C., M.S. Moore, D.A. Sanan, and R.G.W. Anderson. 1991. Reconstitution of clathrin-coated pit budding from plasma membranes. *J. Cell Biol.* 114:881–891.

- Mahaffey, D.T., M.S. Moore, F.M. Brodsky, and R.G.W. Anderson. 1989. Coat proteins isolated from clathrin coated vesicles can assemble into coated pits. *J. Cell Biol.* 108:1615–1624.
- Markovic, I., E. Leikina, M. Zhukovsky, J. Zimmerberg, and L.V. Chernomordik. 2001. Synchronized activation and refolding of influenza hemagglutinin in multimeric fusion machines. *J. Cell Biol.* 155:833–844.
- Melikyan, G.B., S. Lin, M.G. Roth, and F.S. Cohen. 1999. Amino acid sequence requirements of the transmembrane and cytoplasmic domains of influenza virus hemagglutinin for viable membrane fusion. *Mol. Biol. Cell.* 10:1821–1836.
- Nakada, C., K. Ritchie, Y. Oba, M. Nakamura, Y. Hotta, R. Iino, R.S. Kasai, K. Yamaguchi, T. Fujiwara, and A. Kusumi. 2003. Accumulation of anchored proteins forms membrane diffusion barriers during neuronal polarization. *Nat. Cell Biol.* 5:626–632.
- Nguyen, D.H., and J.E. Hildreth. 2000. Evidence for budding of human immunodeficiency virus type 1 selectively from glycolipid-enriched membrane lipid rafts. *J. Virol.* 74:3264–3272.
- Niu, S.L., D.C. Mitchell, and B.J. Litman. 2002. Manipulation of cholesterol levels in rod disk membranes by methyl-beta-cyclodextrin: effects on receptor activation. *J. Biol. Chem.* 277:20139–20145.
- Ono, A., and E.O. Freed. 2001. Plasma membrane rafts play a critical role in HIV-1 assembly and release. *Proc. Natl. Acad. Sci. USA.* 98:13925–13930.
- Prior, I.A., C. Muncke, R.G. Parton, and J.F. Hancock. 2003. Direct visualization of Ras proteins in spatially distinct cell surface microdomains. *J. Cell Biol.* 160:165–170.
- Radhakrishnan, A., and H.M. McConnell. 1999. Condensed complexes of cholesterol and phospholipids. *Biophys. J.* 77:1507–1517.
- Ripley, B.D. 1977. Modeling spatial patterns. *J. R. Stat. Soc. Ser. B.* 39:172–212.
- Ripley, B.D. 1979. Tests of randomness for spatial point patterns. *J. R. Stat. Soc. Ser. B.* 41:368–374.
- Rosenwald, A.G., C.E. Machamer, and R.E. Pagano. 1992. Effects of a sphingolipid synthesis inhibitor on membrane transport through the secretory pathway. *Biochemistry.* 31:3581–3590.
- Roth, M.G., C. Doyle, J. Sambrook, and M.J. Gething. 1986. Heterologous transmembrane and cytoplasmic domains direct functional chimeric influenza virus hemagglutinins into the endocytic pathway. *J. Cell Biol.* 102:1271–1283.
- Ruigrok, R.W., P.C. Krijgsman, F.M. de Ronde-Verloop, and J.C. de Jong. 1985. Natural heterogeneity of shape, infectivity and protein composition in an influenza A (H3N2) virus preparation. *Virus Res.* 3:69–76.
- Sanan, D.A., and R.G.W. Anderson. 1991. Simultaneous visualization of LDL receptor distribution and clathrin lattices on membranes torn from the upper surface of cultured cells. *J. Histochem. Cytochem.* 39:1017–1024.
- Scheiffele, P., A. Rietveld, T. Wilk, and K. Simons. 1999. Influenza viruses select ordered lipid domains during budding from the plasma membrane. *J. Biol. Chem.* 274:2038–2044.
- Sharma, P., R. Varma, R.C. Sarasij, Ira, K. Gousset, G. Krishnamoorthy, M. Rao, and S. Mayor. 2004. Nanoscale organization of multiple GPI-anchored proteins in living cell membranes. *Cell.* 116:577–589.
- Shvartsman, D.E., M. Kotler, R.D. Tall, M.G. Roth, and Y.I. Henis. 2003. Differently anchored influenza hemagglutinin mutants display distinct interaction dynamics with mutual rafts. *J. Cell Biol.* 163:879–888.
- Simons, K., and E. Ikonen. 1997. Functional rafts in cell membranes. *Nature.* 387:569–572.
- Skibbens, J.E., M.G. Roth, and K.S. Matlin. 1989. Differential extractability of influenza virus hemagglutinin during intracellular transport in polarized epithelial cells and nonpolar fibroblasts. *J. Cell Biol.* 108:821–832.
- Sun, X.J., and G.R. Whittaker. 2003. Role for influenza virus envelope cholesterol in virus entry and infection. *J. Virol.* 77:12543–12551.
- Suomalainen, M. 2002. Lipid rafts and assembly of enveloped viruses. *Traffic.* 3:705–709.
- Takeda, M., G.P. Leser, C.J. Russell, and R.A. Lamb. 2003. Influenza virus hemagglutinin concentrates in lipid raft microdomains for efficient viral fusion. *Proc. Natl. Acad. Sci. USA.* 100:14610–14617.
- van Meer, G., and K. Simons. 1982. Viruses budding from either the apical or the basolateral plasma membrane domain of MDCK cells have unique phospholipid compositions. *EMBO J.* 1:847–852.
- Veatch, S.L., and S.L. Keller. 2002. Organization in lipid membranes containing cholesterol. *Phys. Rev. Lett.* 89:268101.
- Veatch, S.L., and S.L. Keller. 2003. Separation of liquid phases in giant vesicles of ternary mixtures of phospholipids and cholesterol. *Biophys. J.* 85:3074–3083.
- Vereb, G., J. Matko, G. Vamosi, S.M. Ibrahim, E. Magyar, S. Varga, J. Szollosi, A. Jenei, R. Gaspar Jr., T.A. Waldmann, and S. Damjanovich. 2000. Cholesterol-dependent clustering of IL-2R α and its colocalization with HLA and CD48 on T lymphoma cells suggest their functional association with lipid rafts. *Proc. Natl. Acad. Sci. USA.* 97:6013–6018.
- Wilson, B.S., J.R. Pfeiffer, and J.M. Oliver. 2000. Observing Fc epsilon RI signaling from the inside of the mast cell membrane. *J. Cell Biol.* 149:1131–1142.
- Wilson, B.S., J.R. Pfeiffer, and J.M. Oliver. 2002. FceRI signaling observed from the inside of the mast cell membrane. *Mol. Immunol.* 38:1259–1268.
- Wilson, B.S., S.L. Steinberg, K. Liederman, J.R. Pfeiffer, Z. Surviladze, J. Zhang, L.E. Samelson, L.H. Yang, P.G. Kotula, and J.M. Oliver. 2004. Markers for detergent-resistant lipid rafts occupy distinct and dynamic domains in native membranes. *Mol. Biol. Cell.* 15:2580–2592.
- Zimmerberg, J. 1993. Simultaneous electrical and optical measurements of individual membrane fusion events during exocytosis. *Methods Enzymol.* 221:99–112.

Hess et al. <http://www.jcb.org/cgi/doi/10.1083/jcb.200412058>**Cell culture, fixation, and immunogold labeling**

Fibroblasts expressing the Japan strain of HA₀, here referred to as HA, (HAB2 cells) were grown as a monolayer on glass coverslips (22 mm square) to 80% confluence. The growth medium was washed with PBS (w/Ca²⁺-Mg²⁺) at RT (~23°C), twice. The cells were washed twice in 0.1 M Hendry's phosphate buffer (1.14 g sodium phosphate monobasic, 1.69 g sodium phosphate dibasic to 100 ml of distilled water final volume, pH 7.35), then fixed with 2% PFA and 0.05% glutaraldehyde in 0.1 M Hendry's phosphate buffer (HPB) for 30 min at RT. The fixative was removed and the cells were washed twice with 0.1 M HPB for 5 min each at RT. The fibroblasts were next rinsed in PBS (w/o Ca²⁺-Mg²⁺) pH 7.4 for 5 min, then blocked in immuno-wash buffer (PBS w/o Ca²⁺-Mg²⁺, 1% BSA, pH 7.4) for 5 min at RT. Cells were incubated with the anti-HA mAb FC-125 for 30–48 min at RT on a rocker plate, and then washed twice with the immuno-wash buffer for 5 min, each at RT. The washes were followed by 30–48 min incubation at RT with a 10-nm-gold-conjugated anti-mouse antibody (Amersham Biosciences) diluted 1:20 in immuno-wash buffer. Alternately, as a control for fixation-induced artifacts, cells were washed and labeled as above but maintained at 4°C without prior fixation. Because our fixation protocol was optimized to minimize damage to the FC125 epitope, fixation was generally done before labeling with antibodies to better preserve membrane structure and HA position. Comparison of the resulting gold densities (see Table I) to published HA densities of HAB2 cells show that a few percent of HA trimers are labeled after fixation. It also suggests little loss with fixation; only ~1/4 of the epitopes labeled before fixation are lost.

Membrane retrieval and preparation for electron microscopy

Formvar-coated and carbon-stabilized 300-mesh copper grids were preincubated for 16 h at 4°C. Just before use, the grids were removed from the refrigerator and floated on a drop of poly-L-lysine (1 mg/ml) for 30 min, then air dried and carefully positioned film-side up on circular pieces of cellulose acetate membrane filter (Osmonics) that had been permeated with the immuno-wash buffer (PBS, Ca²⁺-Mg²⁺-free with 1% BSA) on ice-cold glass. The glass, cellulose filters, and grids were maintained at 4°C. The coverslips containing the gold-labeled cells were quickly drained of excess buffer and placed cell-side down onto the grids. Light pressure was applied to the top of the inverted coverslip for ~10 s. The coverslip was then pulled away from the grids using a set of forceps, lifting from a coverslip corner overhanging the edge of the glass slide. Grids with attached gold-labeled membranes were immediately placed onto drops of cold 0.1 M HPB and then onto drops of 4% glutaraldehyde in 0.1 M HPB at ~0°C for 15 min, and then at RT for 15 min. Steps were performed at RT unless otherwise noted. The grids were subsequently post-fixed in 0.2% osmium tetroxide (aqueous) for 10 min, rinsed three times in HPB, then incubated in 1% aqueous tannic acid for 10 min, rinsed twice with distilled water, incubated in 1% aqueous uranyl acetate for 10 min, rinsed twice with distilled water. Samples were then air dried unless explicitly stated otherwise.

In some cases, critical point drying and methyl cellulose were used to control for effects of the drying process on the observed distribution of gold. For critical point drying, grids with membrane sheets attached were processed as above through the final water wash and then placed in a grid-holder already submerged in H₂O. The grid-holder was carried through a graded series of water-acetone mixtures to a final 100% acetone concentration, which was exchanged 2–3 times. The chamber of the Bal-Tec CPD 030 critical point dryer was filled with fresh, 100% glass-distilled acetone (Electron Microscopy Sciences) and the grid carrier was transferred into the main chamber. At no time in this process was a grid allowed to dry. The critical point dryer was then run in accordance with its directions, the chamber being flushed with liquid CO₂ no less than eight times before the rest of the process was continued. Once the critical point had been reached and the grids removed from the Bal-Tec unit, they were stored over desiccant in a tightly sealed container until they could be viewed in the TEM. For methyl cellulose drying, grids were submerged into methylcellulose, then picked up using small loops of wire and finally air dried.

Cell preparation for thin sectioning

In brief, cells were fixed in 0.25% glutaraldehyde in phosphate buffer for 1 h at RT and then 16–18 h in 2.5% glutaraldehyde at 4°C. Cells were postfixed in 0.2% osmium tetroxide for 30 min at 4°C and stained en bloc with uranyl acetate in sodium acetate buffer. Cells were then rapidly dehydrated in a graded series of increasing alcohol concentration, followed by treatment with absolute alcohol. Cells were then infiltrated with Epon and cured on a level surface at 60°C for 48 h. After curing, the Epon disc was separated from the plastic dish and the fields of interest were selected, removed, and mounted on Epon blanks for sectioning. Ultrathin and serial sections (50 nm) were cut using a UCT Microtome (Leica Microsystems) and collected on 200 mesh copper grids and on formvar-coated/carbon-stabilized single-hole (1 × 2 mm) Cu grids, respectively. Sections were stained with saturated uranyl acetate in 25% methanol and Reynold's lead citrate.

Takeda et al. (2003) found that cholesterol reduction disrupted HA clusters on longer (>50 nm) length scales. Because in our own earlier analyses of thin section data we also thought that these treatments disrupted clusters, we think that this is a natural pitfall of one-dimensional data for two-dimensional structures such as domains. First, our en face views show larger numbers of particles than thin sections, improving the statistical significance of the two-dimensional results relative to the one-dimensional results. Second, in principle, two-dimensional resolution will reduce the chances of having *N* distinguishable particles, randomly distributed over total length *L* of the observation region, appear to be clustered in a single domain of characteristic length *ℓ*: in one dimension, the probability of having *R* particles inside the single domain will be approximately $(\ell/L)^R$ while in two dimensions, this chance reduces to approximately $(\ell/L)^{2R}$ which will be significantly lower if the domain size is smaller than the observed area. Thus, because the thin section results have both reduced dimensionality and smaller numbers of particles, it will be more difficult to resolve whether a distribution is random or nonrandom with the same degree of uncertainty in one dimension as in two dimensions.

Numerical modeling of fluorescence resonance energy transfer efficiency

The expected fluorescence resonance energy transfer (FRET) efficiency was calculated by Monte-Carlo simulation of HA trimers in a 1- μm^2 planar membrane patch. Trimers were distributed with a given density per unit area of typically 2500/ μm^2 , (a) with random position and orientation, excluding the space (8-nm diameter) occupied by other trimers, and (b) in clusters of *n* trimers nucleated from randomly distributed seed trimers with inter-trimer distance $1.1 \cdot d_3$ (where d_3 is the trimer diameter) and the same steric hindrance constraint as in (a). Cy3- or Cy5-conjugated antibody binding to any of the three monomers was simulated by probabilities p_{Cy3} and p_{Cy5} for site occupancy whose amplitude was determined from the experimental antibody titration curve and whose ratio $p_{\text{Cy3}}/p_{\text{Cy5}}$ was fixed to the appropriate experimental value. Accounting for the geometry of the antibody bound to the HA monomer epitope, the antibody binding site was assumed to be on the most exterior side (relative to the trimer center) of the monomer (diameter $d_{\text{mon}} \sim 3.7$ nm), at radius $b = d_{\text{mon}} \cdot (1/2 + 1/\sqrt{3}) = 4.0$ nm from the center of the trimer; the fluorophore was assumed to be fixed at the antibody binding site. The energy transfer rate k_{ET} was calculated between each Cy3 fluorophore (*j*) and every Cy5 fluorophore (*i*) using

$$k_{\text{ET}}^{(j)} = \sum_i \frac{1}{\tau_D} \left(\frac{R_0}{r_{ij}} \right)^\epsilon$$

(Lakowicz, 1983) where τ_D is the donor (Cy3) fluorescence lifetime, r_{ij} is the distance between the j -th Cy3 and the i -th Cy5 fluorophore, and R_0 is 5.3 nm for the Cy3–Cy5 donor-acceptor pair (Ishii et al., 1999). The energy transfer efficiency E for the j -th Cy3 is then given by

$$E^{(j)} = \frac{k_{ET}^{(j)}}{\tau_D^{-1} + k_{ET}^{(j)}}.$$

The expected measured energy transfer E_{exp} is then calculated using

$$F_{cy3}^{pre} = \sum_j 1 - E^{(j)}$$

and

$$F_{cy3}^{post} = \sum_j 1.$$

The probability, p_2 , for a second antibody binding to the same trimer was introduced to simulate the effects of intra-trimer FRET, and used as a fitting parameter when E_{exp} was compared with experiment. Simultaneous antibody binding to all three monomers within a trimer was not considered. 10 identical simulations were run and results averaged to determine mean and SD. The number of trimers per cluster used was $n = 6$ for clustered membrane simulations, and $n = 1$ for unclustered (which gives a random distribution of trimers). Best agreement with measurements was obtained for $p_2 = 0.10 \pm 0.03$, indicating that both intra- and inter-trimer FRET may contribute to the experimental FRET efficiency. The relative proportion of intra- and inter-trimer FRET was determined by forcing $p_2 = 0$ under the same simulation conditions and comparing with $E(p_2 = 0.1)$.

Numerical analysis of particle distributions

Poisson analysis of clustering. The field of each image was divided uniformly into square areas (boxes) and the particles in each box were counted. The frequency distribution of the number of particles per box was then fit using a Poisson distribution:

$$p(x, n) = \frac{A_0 e^{-x} x^n}{n!} \quad (1)$$

where x is the mean of the frequency distribution (the mean number of particles per box), n is the number of particles per box, and the multiplicative constant A_0 was chosen such that the total area under the Poisson distribution was equal to the total area under the measured frequency distribution, summing over all $n \geq 1$. The same box size was used for all images simultaneously and the frequency distributions for the images were summed to create an overall experimental distribution. A field of the same total area with the same total number of particles distributed randomly was also analyzed using the same program by fitting the frequency distribution with Eq. S1. The chi-squared value for the goodness of fit

$$\chi^2 = \sum_i \frac{(O_i - E_i)^2}{E_i} \quad (2)$$

was calculated for both random and experimental distributions, where O is the observed (experimental) frequency and E is the expected (Poisson) frequency. The analysis was repeated as a function of box size for both the measured and random fields of particles. In general, the uncertainty in the frequency value (number of counts) in a given bin of a histogram was estimated as the square root of the number of counts in that bin.

K-test for clustering. The Ripley's K-test (Ripley, 1977, 1979; Prior et al., 2003) was performed, which measures the number of particles within a given radius r of any given labeled HA molecule as follows:

$$L(r) - r = \sqrt{N(r)/\pi D} - \quad (3)$$

where $N(r)$ is the number of particles within a distance r of a given particle, and D is the average particle density per unit area. The function $L(r) - r$ will be positive when clustering occurs, will be zero \pm the confidence interval (CI) for a uniform distribution of particles, and negative for particle distributions which are anti-correlated, on length scale r . Analysis was restricted to length scales ≤ 0.25 times the linear size of the area of interest, wherein the 99% confidence interval (CI₉₉) is given by $\pm 1.68 \cdot \sqrt{A/N_{tot}}$, where A is the image area and N_{tot} is the total number of particles within that area (Ripley, 1979). The values for CI₉₉ were corroborated by simulation results for a random distribution of N_{tot} particles within the same area A . K-test values from different images with the same treatment were normalized by their respective CI₉₉ values before averaging. K-test results reported here use the edge correction according to Diggle (1979), although the results did not differ significantly over the reported range of lengths when other edge correction methods were used. Variation in $L(r) - r$ among images with the same treatment may indicate different patterns of clustering present simultaneously within the observed membrane areas. Although we do not pursue such matters, analysis of such variation might in principle allow distinction between multiple types of membrane protein microdomains.

Monte-Carlo simulation of membrane HA and gold particle distribution

Experimental results for different treatments were compared with random and clustered distributions generated by Monte-Carlo computer simulation. Clustered membrane distributions were simulated by distributing seed trimers randomly within a planar area and then adding clustered trimers in molecular contact to a randomly chosen seed trimer or clustered trimer. Trimers were treated as hard cylinders with a radius d_m . The number of seed trimers was fixed arbitrarily to the total number of trimers divided by 50. The ratio of clustered to total trimers f_{clust} was varied by first distributing a given number of seed and clustered trimers and then adding randomly distributed trimers to yield the desired ratio and an average trimer density per unit area (D_{avg}). The value of D_{avg} was typically fixed to 2,500 trimers/ μm^2 , which is the center of the range $(2.9 \pm 1.9 \times 10^3 \text{ trimers}/\mu\text{m}^2)$ measured previously for the same cell type (Ellens et al., 1990). To simulate the observed distribution of gold particles, the probability of a given trimer being labeled by a gold-linked antibody, or capture ratio (κ), was incorporated into the model. Gold particles were placed directly above the center of a labeled HA trimer. Typically, simulations distributed 10^4 trimers per run within a membrane region of $2 \times 2 \mu\text{m}$. Unless otherwise noted, resulting nearest neighbor histograms and gold particle distributions were calculated for 100 runs under a given set of conditions and saved in a database for repeated statistical analysis.

Fitting of measured distributions with simulation results

The procedure for fitting is detailed as follows. (1) Simulations were run repeatedly (typically 100 runs) under a given set of parameters (f_{cluster} , κ , d_{min}). (2) The average and SD of the measured histograms (nearest neighbor, angular neighbor) and SD were calculated from repeated simulation runs with the given parameters. (3) A database was created containing the average histograms and SDs for all simulated conditions. (4) The squared difference between the measured and a given average simulation was calculated and used to calculate a weighted χ^2_w using the following formula:

$$\chi^2_w = \sum_i w_i \frac{(O_i - E_i)^2}{1 + E_i} / \sum_i w_i \quad (4)$$

where O_i and E_i are the i -th bin of the measured and simulated histograms, respectively, and $w_i = \sqrt{O_i}$ is a weighting factor. (5) The set of conditions which yielded the minimum χ^2_w for a given membrane treatment was defined as the best fit. (6) The dependence of χ^2_w at and near the minimum of χ^2_w as a function of the simulation parameters was determined. From the width of the minimum of χ^2_w as a function of a particular variable x , the uncertainty in x is estimated as the distance along the x axis from the minimum which produced a factor of two higher value for χ^2_w .

Estimated bounds on length scales accessible to FRET and electron microscopy

We choose the upper bound of the length scale based on a conservative attempt to avoid boundary effects at the edges of the images; we therefore refrain from considering length scales larger than 1/4 the length of the image diagonal ($\sim 3.6 \mu\text{m}/4 = 0.9 \mu\text{m}$). For EM, the lower limit of reliable distances (20 nm) is given by twice the diameter of a gold particle, to avoid any potential artifacts due to steric interactions. The length scales accessible to our FRET measurements were estimated using the Förster equation and published value of R_0 to calculate the inter-trimer distance corresponding to the minimum and maximum values of energy transfer observed experimentally between donor and acceptor. Thus within the accessible length scales, the observed distribution of HA is inconsistent with models that predict partitioning of proteins into lipid domains and their random mixing therein.

Artifacts

Antibody and fixation artifacts. It is possible that the multivalent antibodies used to label HA in these experiments could bind to one monomer within two different HA trimers and induce clustering of HA; then one expects more clustering in membranes treated with antibody before fixation than in those fixed before labeling. No significant differences in the degree or size of clustering were observed between cells fixed before labeling and data from controls labeled with antibody before fixation, indicating (1) that the degree of antibody-induced clustering is low; and (2) that fixation did not induce much clustering. In agreement with this idea, studies by Prior et al. (2003) indicate that antibody-induced clustering can be induced when fixation is done with PFA without glutaraldehyde, but that such induced clustering occurs on length scales from 10–30 nm. However, we fix using both PFA and glutaraldehyde. Finally, this putative mechanism could result from either primary or secondary antibody. Our FRET measurements and modeling indicate that the probability of intra-trimer energy transfer due to multiple fluorescently labeled primary antibodies binding to the same HA trimer is low (less than $\sim 10\%$), which would be necessary to form antibody-induced aggregates larger than dimer. Any residual antibody cross-linking would thus only result in aggregates on the scale of a dimer of trimer. Secondary antibody-induced clustering could also occur, but we only label $<10\%$ of our trimers, so most are unlabeled by a gold particle, so the fraction having two bound to the given trimer would likely be much lower (i.e., $<1\%$).

It is also possible that fixation resulted in a nonspecific packing of HA, if there was a preference of glutaraldehyde for HA or for protein over lipid. Upon adding fixative, the glutaraldehyde could bind each HA trimer with one end, leaving effectively “sticky” HAs. Then in the ensuing time HAs could collide with each other and stick, leaving the nonrandom pattern we see. But small changes in lipid composition altered the close packing of HA, as measured by FRET; if packing were instead dependent upon fixation one would have the same pattern. Also, when membrane lipids are removed, the long-scale pattern of packing is also altered, contrary to the expectation of little effect if the clustering is due to fixation artifacts. Furthermore, changing the order of fixation and labeling would have altered the pattern of clustering, but this was not seen. Although the fractal dimension observed $D \sim 1.50\text{--}1.95$ (using the slope of the K-test $N(r)$ as a function of r , plotted on a log–log scale) is for some images consistent with diffusion-limited fast aggregation, the dimension D shows enough variability to disfavor the idea that diffusion-limited fast aggregation is the consistent, primary force leading to the observed clustering. Finally, it has been observed that several other proteins visualized by immunogold electron microscopy after fixation with glutaraldehyde do not show the same pattern of clustering, and in some cases are entirely unclustered (Prior et al., 2003). Thus, it seems unlikely (but not impossible) that glutaraldehyde is the primary reason for the observed pattern of clustering, probably because it is indiscriminate in its binding partner.

Gold artifacts. It is possible for two gold particles to appear closer to one another than 10 nm; gold particles were observed occasionally to appear to touch each other (i.e., ≤ 10 nm center-to-center distance), although the fraction of nearest neighbor distances greater than 10 nm is 98.2%. This closeness may actually be gold in different z -planes. To test this, we made stereo-pairs of immunogold-labeled membranes: whenever gold particles touched or overlapped in a single image, they were seen in stereo as being adjacent to each other on a curved piece of membrane. However, replacement of these data points did not significantly change the outcome due to their low abundance. Furthermore, we estimated that out-of-plane height variations were less than 20 nm. Thus, the error contribution of this artifact to our analysis of the gold positions is not significant. Furthermore, our quantitative model for the nearest neighbor histogram based on Monte-Carlo simulation shows excellent agreement between measurement and theory with trimers distributed within a plane.

Drying artifacts. Similar patterns of membrane clustering were revealed by K-test analysis of samples which were critical point dried (Fig. 5 C), indicating that drying artifacts are not a significant explanation of the observed pattern of clustering.

References

- Diggle, P.J. 1979. On parameter estimation and goodness-of-fit testing for spatial point patterns. *Biometrics*. 35:87–101.
- Ellens, H., J. Bentz, D. Mason, F. Zhang, and J.M. White. 1990. Fusion of influenza hemagglutinin-expressing fibroblasts with glycoprotein-bearing liposomes: role of hemagglutinin surface density. *Biochemistry*. 29:9697–9707.
- Ishii, Y., T. Yoshida, T. Funatsu, T. Wazawa, and T. Yanagida. 1999. Fluorescence resonance energy transfer between single fluorophores attached to a coiled-coil protein in aqueous solution. *Chem. Phys.* 247:163–173.
- Lakowicz, J.R. 1983. Principles of fluorescence spectroscopy. Plenum Press, NY. 496 pp.
- Prior, I.A., C. Muncke, R.G. Parton, and J.F. Hancock. 2003. Direct visualization of Ras proteins in spatially distinct cell surface microdomains. *J. Cell Biol.* 160:165–170.
- Ripley, B.D. 1977. Modelling spatial patterns. *J. R. Stat. Soc. Ser. B.* 39:172–192.
- Ripley, B.D. 1979. Tests of randomness for spatial point patterns. *J. R. Stat. Soc. Ser. B.* 41:368–374.
- Takeda, M., G.P. Leser, C.J. Russell, and R.A. Lamb. 2003. Influenza virus hemagglutinin concentrates in lipid raft microdomains for efficient viral fusion. *Proc. Natl. Acad. Sci. USA.* 100:14610–14617.